



This is a repository copy of *N-1 evaluation of integrated electricity and gas system considering cyber-physical interdependence*.

White Rose Research Online URL for this paper:
<https://eprints.whiterose.ac.uk/id/eprint/227997/>

Version: Accepted Version

Article:

Zhang, S. orcid.org/0000-0003-4707-3904, Zhang, X. orcid.org/0000-0002-6063-959X, Zhang, R. et al. (2 more authors) (2025) N-1 evaluation of integrated electricity and gas system considering cyber-physical interdependence. IEEE Transactions on Smart Grid. p. 1. ISSN 1949-3053

<https://doi.org/10.1109/tsg.2025.3578271>

© 2025 The Authors. Except as otherwise noted, this author-accepted version of a journal article published in IEEE Transactions on Smart Grid is made available via the University of Sheffield Research Publications and Copyright Policy under the terms of the Creative Commons Attribution 4.0 International License (CC-BY 4.0), which permits unrestricted use, distribution and reproduction in any medium, provided the original work is properly cited. To view a copy of this licence, visit <http://creativecommons.org/licenses/by/4.0/>

Reuse

This article is distributed under the terms of the Creative Commons Attribution (CC BY) licence. This licence allows you to distribute, remix, tweak, and build upon the work, even commercially, as long as you credit the authors for the original work. More information and the full terms of the licence here:
<https://creativecommons.org/licenses/>

Takedown

If you consider content in White Rose Research Online to be in breach of UK law, please notify us by emailing eprints@whiterose.ac.uk including the URL of the record and the reason for the withdrawal request.



eprints@whiterose.ac.uk
<https://eprints.whiterose.ac.uk/>

N-1 Evaluation of Integrated Electricity and Gas System Considering Cyber-Physical Interdependence

Suhan Zhang, *Member, IEEE*, Xin Zhang, *Senior Member, IEEE*, Rui Zhang, Wei Gu, *Senior Member, IEEE*, Ge Cao, *Member, IEEE*

Abstract--The deepening digitalisation of infrastructure has significantly increased the interconnection between power systems (PS) and gas systems (GS), rendering integrated electricity and gas systems (IEGS) more vulnerable to cyber-physical contingencies (CPC). This paper pioneers the investigation into N-1 contingency evaluation for cyber-physical IEGS to identify critical failures that pose threats to operational security. To accurately model various CPCs in IEGS, we introduce a nonlinear partial differential-algebraic equation (PDAE) model, which redefines CPCs as discontinuities and abrupt changes in simulation boundaries. We further propose a variable-coefficient analytical method (VC-AM) designed to robustly and efficiently handle these reformulated boundaries during CPC simulations. Building on this foundation, an N-1 evaluation framework is established to explore the contingency impact propagation and detect resultant violations, incorporating several performance indexes to quantify and rank the impacts of diverse contingencies. Case studies reveal that cyber-physical interdependence notably amplifies the effects of contingencies, underscoring the potential of VC-AM for real-time N-1 evaluation. In contrast, traditional methods are hindered by high computational complexity and convergence challenges.

Index Terms--Cyber-physical contingency, integrated electricity and gas system, N-1 evaluation, variable-coefficient analytical method, cyber physical interdependence.

NOMENCLATURE

A. Abbreviations

| | |
|--------|---|
| PS/GS | Power system/gas system |
| IEGS | Integrated electricity and gas system |
| CPPS | Cyber-physical power system |
| CPC | Cyber-physical contingency |
| PDE | Partial differential equation |
| PDAE | Partial differential-algebraic equation |
| FDM | Finite difference method |
| MOC | Method of characteristics |
| VC-AM | Variable-coefficient analytical method |
| GT/P2G | Gas turbine/power-to-gas |
| PI | Performance index |
| MRD | Mean relative difference |

This work was supported in part by the U.K. Research and Innovation Future Leaders Fellowship ‘Digitalisation of Electrical Power and Energy Systems Operation’ under Grant MR/W011360/2 and in part by the Royal Society International Exchanges under Grant IEC\NSFC\242449.

S. Zhang, X. Zhang (Corresponding author) are with the School of Electrical and Electronic Engineering, The University of Sheffield, S1 3JD Sheffield, U.K. (e-mails: {suhan.zhang, xin.zhang1}@sheffield.ac.uk).

R. Zhang is with the National Energy System Operator NESO, RG41 5BN Wokingham, U.K. (e-mail: rui.zhang@nationalenergyso.com)

W. Gu is with the School of Electrical Engineering, Southeast University, 210000 Nanjing, China. (e-mail: wgu@seu.edu.cn)

G. Cao is with the School of Electrical Engineering, Xi’an University of Technology, 710000 Xi’an, China. (e-mail: caogeseu@126.com)

| | |
|-----|-----------------------------|
| LRD | Largest relative difference |
| CIS | Central implicit scheme |
| EIS | Euler implicit scheme |

B. Sets and Symbols

| | |
|-----------|--|
| $V/E/G$ | Set of nodes/branches/graph |
| Γ | Set of time flags |
| elg | Superscript of variables in PS/GS |
| clp | Subscript of variables in cyber/physical layer |
| gt/pg | Symbol of variables in GT/P2G |
| i/o | Superscript of inlet/outlet variables |
| min/max | Subscript of minimum/maximum values |
| $rate$ | Subscript of rated values |
| nd | Subscript of node variables in GS |
| $leak$ | Subscript of leakage variables |

C. Main Parameters

| | |
|-------------------------------|---|
| G/B_{ij} | Conductance/susceptance between buses i and j |
| D/S | Diameter/cross-section area of pipe |
| λ/L | Friction factor/length of pipe |
| t_f | Fault time |
| K_{cp} | Compression ratio |
| H_g/c | Calorific value/sound speed |
| η | Conversion efficiency |
| A/X | Adjacency matrix/communication link |
| S_l/d | Cross-section area/diameter of leakage |
| p_d/p_{cr} | Atmospheric/critical pressure |
| ξ/γ | Orifice loss/adiabatic coefficient |
| $\Delta t/\Delta x$ | Time step/spatial step |
| N_b/N_g | Number of pipes/nodes |
| $\delta_{1n}/\delta_{2n}/F_n$ | Constant parameters for simplification |

D. Main Variables

| | |
|---------------------|--|
| P_G/Q_G | Active/reactive power generation |
| P_L/Q_L | Active/reactive power load |
| U/θ | Voltage magnitude/phase angle |
| $P_l/Q_l/S_l$ | Line active/reactive/apparent power flow |
| p/q | Pressure/mass flow rate |
| w | Average flow velocity |
| u_n/g_n | Coefficients for simplification |
| J_1-J_4 | Transfer matrixes in VC-AM |
| γ_p/γ_q | Components of p/q determined by initial conditions |
| ξ_p/ξ_q | Components of p/q determined by initial conditions and previous boundaries |

I. INTRODUCTION

A. Background and Motivations

THE advancement of information and communications technology has catalysed the digital transformation of

power and energy systems, leading to deepening cyber-physical interdependence between traditionally heterogeneous systems such as power system (PS) and gas system (GS). This interdependence allows for coordinated operation and control within an integrated electricity and gas system (IEGS), promoting cleaner energy and more flexible system management [1]. Since 2018, the European Union has been actively supporting this trend through policies and legislative measures aimed at accelerating energy system integration and digitalisation [2]. More recently, in 2024, the UK government has taken steps to strengthen gas-powered stations for a more secure energy supply [3] and has established the National Energy System Operator by merging the Electricity System Operator with National Gas Transmission, responsible for both power and gas systems to enhance collaborative operations within the IEGS [4].

While these developments present substantial opportunities, the bidirectional coupling between PS and GS facilitates the cross-system contingency propagation, and this cyber-physical interdependence is exacerbated by deep digitalisation, significantly amplifying the integrated system risks [5]. In 2018, a cyberattack on U.S. companies' gas data providers led to unexpected power outages [6]-[7], while severe storm weather in Wales caused large-scale power failures in 2024, subsequently disrupting gas, heating, and water services due to communication losses [8]. These incidents emphasise the critical need for power and gas utility operators to develop precise contingency models and assess potential risks to mitigate possible losses and enhance operational security considering cyber-physical interdependence.

B. Literature Review

N-1 redundancy is a preventive principle for cyber-physical power system (CPPS), designed to ensure the system maintains secure operation following the occurrence of any single-component failure. The basis of this principle is the contingency simulation and evaluation, with related studies falling into two categories. The first category leverages graph theory to model CPPS based on the topological connections within the PS and corresponding communication network, assessing the impact of cyber-physical contingencies (CPCs) according to the topological connectivity. The second category focuses on the physical attributes of the system, modelling the CPPS accordingly and evaluating CPCs by examining post-contingency energy flow distribution. In the graph-theory-based approach, reference [9] combined graph theory with Markov chains to emulate state transitions between the PS and communication network. Reference [10] accommodated business differences and advanced the traditional graph theory model with different edge weights. Reference [11] dynamically updated the security indexes and evaluated the security level of the given CPC settings based on a stochastic Bayesian network. The second category, which models the CPPS according to its physical properties, analyses the detailed availability of substation equipment and communication latency under contingencies. Reference [12] developed an intricate substation model and quantified CPC impacts as expected energy not

supplied and resultant load loss with Markov chains. References [13]-[14] applied network calculus to examine changes in communication network latency during CPCs. Reference [15] performed vulnerability analysis on cascading failures, statistically analysing limit-exceeding states during fault propagation to quantify CPC impacts. Reference [16] explored CPPS vulnerabilities under cyber-attacks using a percolation-based methodology, addressing both equipment and network vulnerabilities. Reference [17] simulated the cascading effects of CPCs in power systems via iterative power flow calculations, post-contingency routing strategies of communication network were incorporated.

The aforementioned studies mainly focus on quantifying the impacts of specific CPCs in the PS, while the overall assessment across diverse CPCs like N-1 evaluation for the whole CPPS was limited. Moreover, they have paid relatively little attention to electricity-gas CPCs despite reported incidents [6]-[7]. Different from that in the PS, the intricate physical coupling between the PS and GS introduces a more multitude of contingency types and impact propagation pathways, while the cyber-physical coupling across the PS and GS further increases system interdependence and introduces new risk propagation through the communication network, significantly complicating the cyber-physical security analysis of IEGS. The challenges are threefold. Firstly, by analogy to the PS, most studies adopt similar methods to model contingencies in IEGS, such as topological disconnection or node removal [18]. This assumption is impractical for the IEGS because gas state propagation changes slowly rather than instantaneously during a contingency, thereby propagating to the PS as a gradual process rather than a sudden change and altering its state distribution over time. Secondly, while static N-1 evaluation of PS at various time intervals are treated as relatively independent and described by algebraic equations, the GS model is governed by partial differential-algebraic equations (PDAEs). Contingencies within the GS can cause abrupt changes in slowly varying states, leading to discontinuities in electricity-gas integrated simulation settings. Traditional numerical methods, such as finite difference methods (FDM) and method of characteristics (MOC) [19], struggle with addressing these discontinuities and ensuring convergence when solving PDAEs [20]. Thirdly, given the interrelated nature of gas states across multiple time intervals [21], the effects of CPCs on security issues in IEGS tend to diffuse over time. Consequently, the N-1 evaluation of the IEGS becomes a multi-time-interval computation problem, characterised by a significant computational burden. This complexity makes existing solutions far from meeting real-time requirements.

C. Contributions and Paper Organisation

To address these mentioned gaps, this paper introduces an N-1 contingency evaluation framework to identify and rank critical CPCs within IEGS. This framework considers various types of CPCs in detail to capture their dynamics and impacts. A variable-coefficient analytical method (VC-AM) is tailored to ensure efficiency and convergence of the N-1 contingency simulation. The main contributions of this paper are outlined as

follows:

(1) We present the nonlinear PDAE models tailored to various CPCs in IEGS. These models accurately capture the time-varying characteristics of contingency features and describe state mutations caused by contingencies through the reformulation of simulation boundaries.

(2) We propose a novel VC-AM for CPC simulation. The VC-AM transforms the original nonlinear PDE into a variable-coefficient PDE and avoids PDE discretisation, significantly improving the simulation efficiency and convergence rate.

(3) To identify the critical CPCs, we develop an N-1 contingency evaluation framework for cyber-physical IEGS that considers multi-timescale properties. This framework incorporates several performance index (PI) for quantitative evaluation and ranking of CPCs in IEGS.

The remainder of this paper is as follows. The model of IEGS is introduced in Section II. The CPCs in IEGS are modelled in Section III. Section IV presents the simulation procedure and PI of N-1 evaluation of cyber-physical IEGS. Case studies and conclusions are given in Sections V and VI, respectively.

II. INTEGRATED ELECTRICITY AND GAS SYSTEM

The cyber-physical architecture of the IEGS is depicted in Fig. 1. For clarification, ‘bus’ and ‘node’ refer to the physical nodes of the PS and GS, ‘line’ and ‘pipe’ refer to the physical branches of the PS and GS. Within this architecture, the physical layer integrates the PS and GS, which are bidirectionally coupled with gas turbines (GTs) and power-to-gas (P2G) installations. The cyber layer supports intra-system communication for operational independence. All communication nodes within the IEGS are electrically powered, establishing a bidirectional coupling between the cyber and physical layers.

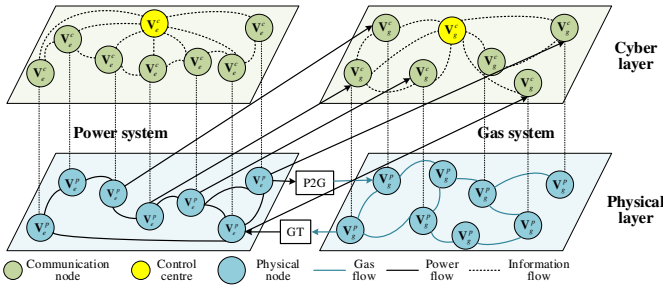


Fig. 1. Cyber-physical architecture of an IEGS.

A. Model of Physical Layer

1) Power System

In real-world N-1 contingency evaluation, the power flow equations are widely adopted to characterise the electric state distribution in the PS, as shown below.

$$\begin{cases} P_{G,i} - P_{L,i} = U_i \sum_j U_j (G_{ij} \cos \theta_{ij} + B_{ij} \sin \theta_{ij}) \\ Q_{G,i} - Q_{L,i} = U_i \sum_j U_j (G_{ij} \sin \theta_{ij} - B_{ij} \cos \theta_{ij}) \end{cases} \quad i, j \in \mathbf{V}_e^p \quad (1)$$

$$\begin{cases} P_{l,ij} = U_i U_j (G_{ij} \cos \theta_{ij} + B_{ij} \sin \theta_{ij}) - G_{ij} U_i^2 \\ Q_{l,ij} = U_i U_j (G_{ij} \sin \theta_{ij} - B_{ij} \cos \theta_{ij}) + B_{ij} U_i^2 \end{cases} \quad i, j \in \mathbf{V}_e^p \quad (2)$$

where \mathbf{V}_e^p is the set of physical buses in the PS; P_G and P_L are the active power generation and load, MW; Q_G and Q_L are the reactive power generation and load, MVar; U is the voltage magnitude, p.u.; θ are the phase angle, rad; B_{ij} and G_{ij} are the conductance and susceptance between buses i and j , p.u.; P_l is the active line power flow, MW; Q_l is the reactive line power flow, MVar.

2) Gas System

The gas flow distribution along the pipe is described by fluid dynamic equations. Assuming the uniform parameter distribution along the pipe and isothermal transportation process, the commonly used GS model is expressed as:

$$\frac{\partial p_{x,t}}{\partial t} + \frac{c^2}{S} \frac{\partial q_{x,t}}{\partial x} = 0, \quad \frac{\partial p_{x,t}}{\partial x} + \frac{1}{S} \frac{\partial q_{x,t}}{\partial t} + \frac{\lambda c^2 q_{x,t} |q_{x,t}|}{2DS^2 p_{x,t}} = 0 \quad (3)$$

where c is the sound speed, 340m/s; D is the pipe diameter, m; λ is pipe friction factor; $q_{x,t}$ is the pipe mass flow rate, kg/s; $p_{x,t}$ is the pipe pressure, Pa; S is the pipe cross-section area, m².

Besides, the gas flow at junctions should satisfy mass conservation and pressure continuity equations, as follows.

$$\sum_b q_{b,x=L} - \sum_j q_{j,x=0} = q_{nd,k} \quad b \in \mathbf{E}_{g,k}^{p,o}, j \in \mathbf{E}_{g,k}^{p,i}, k \in \mathbf{V}_g^p \quad (4)$$

$$p_{b,L} = p_{nd,k}, p_{n,0} = K_{cp,k} p_{nd,k} \quad b \in \mathbf{E}_{g,k}^{p,o}, n \in \mathbf{E}_{g,k}^{p,i}, k \in \mathbf{V}_g^p \quad (5)$$

where $\mathbf{E}_{g,k}^{p,o}$ and $\mathbf{E}_{g,k}^{p,i}$ are the sets of pipes ending and starting at node k ; q_{nd} is the node mass flow rate, kg/s; p_{nd} is the node pressure, Pa; L is the pipe length, m; $K_{cp,k}$ is the compression ratio if node k is a compressor, else, $K_{cp,k}=1$.

3) Coupling Units

In this paper, the P2G and GT are considered to couple the PS and GS physically. The GT is treated as the generator bus in the PS and load node in the GS. The P2G is treated as the electric load in the PS and the source node (with adjustable flow rate) in the GS. Their models are shown below.

$$P_{gt} = \eta_{gt} q_{gt} H_g, \quad P_{pg} = q_{pg} H_g / \eta_{pg} \quad (6)$$

where η_{gt} and η_{pg} are the energy conversion efficiency of the GT and P2G; H_g is the calorific value of the gas flow, MW/kg; P_{gt} is the active power generation of GT, MW; P_{pg} is the active power consumption of P2G, MW; q_{gt} is the consumed gas flow of GT, kg/s; q_{pg} is the generated gas flow of P2G, kg/s.

B. Model of Cyber Layer

As shown in Fig. 1, a typical cyber layer of the PS and GS contains a control centre and multiple communication nodes connected through wireless and fiber-optic lines. The communication nodes upload measurements to the control centre, while the control centre receives measurements and delivers control command to the communication nodes. Let $\mathbf{G} = \{\mathbf{V}, \mathbf{E}\}$ be the graph of a communication network, $(i, j) \in \mathbf{E}$ indicates that there is a communication link between nodes i and j . Then, the topology of a communication network \mathbf{G}^c can be described by the adjacency matrix \mathbf{A}^c , whose elements are

expressed as:

$$A_{ij}^c = \begin{cases} 1 & (i, j) \in \mathbf{E}^c \\ 0 & (i, j) \notin \mathbf{E}^c \end{cases} \quad (7)$$

Based on the adjacency matrix \mathbf{A}^c , the link set \mathbf{X}^c between control centres and communication nodes can be built with path search algorithms. Let the control centre and communication node be i and j , the link set \mathbf{X}_{ij}^c can be expressed as:

$$\mathbf{X}_{ij}^c = \{X_{ij}^{c,(1)}, X_{ij}^{c,(2)}, \dots, X_{ij}^{c,(n)}\} \quad (8)$$

$$\begin{cases} X_{ij}^{c,(n)} = \{A_{ik}^c, A_{ka}^c, \dots, A_{am}^c, A_{mj}^c\} \\ A_{ik}^c, A_{ka}^c, \dots, A_{am}^c, A_{mj}^c \neq 0 \end{cases} \quad (9)$$

Here, $X_{ij}^{c,(1)}$ is the primary link corresponding to the shortest path between nodes i and j , which is determined by the Dijkstra algorithm. $X_{ij}^{c,(2)}$ to $X_{ij}^{c,(n)}$ are backup links in case of contingency. In this paper, we use BA scale-free network to generate cyber networks, and then generate the communication links using (7)-(9).

C. Model of Cyber-Physical Interdependence

In the IEGS, cyber-physical interdependence can be divided into three categories. The first category refers to scenarios where the failure of physical components will cause their corresponding cyber components to lose functionality due to power loss. This can be represented as:

$$i \notin \mathbf{V}^p \Rightarrow i \notin \mathbf{V}^c \quad (10)$$

It should be noted that CCs are typically equipped with backup batteries to address potential faults, thus they do not fall under this category of interdependence.

The second category applies to critical physical nodes $\mathbf{V}^{p,crit}$, such as primary power plants and gas sources, transformers and compressors, and important loads. These facilities are usually equipped with local controllers in case of cyber contingency. Thus, disconnecting the corresponding communication nodes does not affect their normal operation.

$$i \notin \mathbf{V}^c \Rightarrow \text{node } i \text{ operate normally, } i \in \mathbf{V}^{p,crit} \quad (11)$$

The third category occurs at ordinary physical nodes without local controller. When cyber contingency occurs at these nodes, their corresponding physical components will lose controllability. This can be represented as:

$$i \notin \mathbf{V}^c \Rightarrow \text{node } i \text{ loses control, } i \notin \mathbf{V}^{p,crit} \quad (12)$$

III. PRELIMINARIES

A. Cyber-Physical Contingencies in IEGS

N-1 analysis aims to evaluate whether a single-component failure could cause overloading, overvoltage, or overpressure in other components during its impact propagation throughout the integrated system. In IEGS, single-component failures primarily manifest as node or branch failures across cyber and physical layers, as summarised in TABLE I. At the cyber layer, node and branch failures in both the PS and GS exhibit analogous characteristics, corresponding to outages of

communication nodes and links, respectively. At the physical layer, node failures differ between the two subsystems. Node failures in the PS involve generator and important electric load outages, while those in the GS pertain to gas source, compressor and important gas load outages. As for the branch failures, those in the PS typically represent transformer failures and transmission line outages, whereas fully analogous failures in the GS rarely occur. Instead, pipe failures in the GS are predominantly caused by leakages rather than full disconnection.

TABLE I Cyber-Physical CONTINGENCY CHECKLIST IN IEGS

| | PS | GS |
|----------------|-------------------------|----------------------------------|
| Node failure | Generator | Gas source |
| | Important electric load | Important gas load |
| | Communication node | Compressor Communication node |
| Branch failure | Transmission line | Gas pipe leakage |
| | Transformer | Communication link |
| | Communication link | Communication link |

B. Simulation Boundaries in N-1 Evaluation

The essence of N-1 analysis is to repeatedly solve the energy flow equations under given operating strategies and contingency information to evaluate the system performance. Thus, determining the simulation boundaries of different components under normal and contingency conditions is a preliminary step in N-1 analysis.

Under normal conditions, the simulation boundaries for PS include active and reactive power consumption at PQ buses, active power generation and voltage magnitude at PV buses, voltage magnitude and phase angle at the slack bus, transformer states, and network topology. As for the GS, the simulation boundaries encompass pressure at source nodes, mass flow rates at load nodes, compressor states, and network topology. Under contingency conditions, these boundaries will undergo changes and be discussed below. For simplification, we assume t_f as the fault time and pre as the superscript of boundaries under normal states.

1) Cyber Contingency in the PS

A communication node failure in the PS will directly result in its removal from the communication network, causing changes of \mathbf{G}_e^c . If this removal leads to a communication link disconnection between the CC and communication nodes, it will further trigger a cyber-cyber contingency. Moreover, if the failed communication node is connected to an electric bus, it will cause contingency propagation from the cyber layer to the physical layer and alter the boundary of the corresponding physical node. There are different controllability impacts of the cyber contingency on various power system components, which are classified as follows.

For autonomous PV buses, local controller like automatic voltage regulators can maintain voltage level in case of communication failures, which is expressed as:

$$i \notin \mathbf{V}_e^c \Rightarrow \begin{cases} P_{G,i,t} = P_{G,i,t}^{pre} \\ U_{i,t} = U_{i,t}^{pre} \\ Q_{G,i,t}, \theta_{i,t} \text{ to be determined} \end{cases}, \quad \begin{matrix} i \in \mathbf{V}_{e,PV}^{p,crit} \\ t > t_f \end{matrix} \quad (13)$$

For communication-dependent PV buses, their local controllers may lack autonomous voltage regulation logic. These PV buses will maintain their pre-contingency levels of active and reactive power outputs and are assumed to become equivalent PQ buses in the event of communication failures. The impact of this CPC propagation can be expressed as:

$$i \notin \mathbf{V}_e^c \Rightarrow \begin{cases} P_{G,i,t} = P_{G,i,t_f} \\ Q_{G,i,t} = Q_{G,i,t_f} \\ U_{i,t}, \theta_{i,t} \text{ to be determined} \end{cases}, \quad i \notin \mathbf{V}_{e,PV}^{p,crit}, t > t_f \quad (14)$$

For important PQ buses, those with local controllers can operate normally under cyber contingency, while the others will lose the control capability, as shown below.

$$i \notin \mathbf{V}_e^c \Rightarrow \begin{cases} P_{L,i,t} = P_{L,i,t}^{pre} \\ Q_{L,i,t} = Q_{L,i,t}^{pre} \\ U_{i,t}, \theta_{i,t} \text{ to be determined} \end{cases}, \quad i \in \mathbf{V}_{e,PQ}^{p,crit}, t > t_f \quad (15)$$

$$i \notin \mathbf{V}_e^c \Rightarrow \begin{cases} P_{L,i,t} = P_{L,i,t_f} \\ Q_{L,i,t} = P_{L,i,t_f} \\ U_{i,t}, \theta_{i,t} \text{ to be determined} \end{cases}, \quad i \notin \mathbf{V}_{e,PQ}^{p,crit}, t > t_f \quad (16)$$

Transformers are critical components in the PS, and thus we assume that they are equipped with local controllers and can maintain normal operation in case of communication node failure. A communication link failure in the PS will directly result in the disconnection between two adjacent nodes, which is expressed as:

$$(i, j) \notin \mathbf{E}_e^c \Rightarrow A_{e,ij,t_f}^c = 0 \quad (17)$$

If this communication link failure further causes a disconnection between the control centre and communication nodes, it will further trigger a cyber-cyber contingency and result in corresponding communication nodes to be cut off.

2) Cyber Contingency in the GS

Similar to that of the PS, CPC induced by communication node failures will not affect the gas sources with local controller, while those without local controller will lose the controllability of gas pressure regulation and become equivalent load nodes. This type of contingency can be expressed as:

$$i \notin \mathbf{V}_g^c \Rightarrow \begin{cases} p_{nd,i,t} = p_{nd,i,t}^{pre} \\ q_{nd,i,t} \text{ to be determined} \end{cases}, \quad i \in \mathbf{V}_{g,sr}^{p,crit}, t > t_f \quad (18)$$

$$i \notin \mathbf{V}_g^c \Rightarrow \begin{cases} q_{nd,i,t} = q_{nd,i,t_f} \\ p_{nd,i,t} \text{ to be determined} \end{cases}, \quad i \notin \mathbf{V}_{g,sr}^{p,crit}, t > t_f \quad (19)$$

For important load nodes in the GS, the cyber contingency model is similar to (15) and (16), which is expressed as:

$$i \notin \mathbf{V}_g^c \Rightarrow \begin{cases} q_{nd,i,t} = q_{nd,i,t}^{pre} \\ p_{nd,i,t} \text{ to be determined} \end{cases}, \quad i \in \mathbf{V}_{g,ld}^{p,crit}, t > t_f \quad (20)$$

$$i \notin \mathbf{V}_g^c \Rightarrow \begin{cases} q_{nd,i,t} = q_{nd,i,t_f} \\ p_{nd,i,t} \text{ to be determined} \end{cases}, \quad i \notin \mathbf{V}_{g,sr}^{p,crit}, t > t_f \quad (21)$$

Also, compressors are usually deployed at key locations with local controller. We assume that they can operate normally under communication node failure.

For communication link failures in the GS, we adopt the same expression to model its impact, as shown below.

$$(i, j) \notin \mathbf{E}_g^c \Rightarrow A_{g,ij,t_f}^c = 0 \quad (22)$$

3) Physical Contingency in the PS

The failure of a generator or important electric load will result in its removal from the PS, thereby altering the network topology \mathbf{G}_e^p and eliminating the associated simulation boundary during N-1 analysis. If the affected electric bus supplies power to a communication node, this initiates a contingency propagation from the physical layer to the cyber layer. Such a CPC propagation will subsequently force the corresponding communication node to be cut off, which can be modelled as:

$$i \notin \mathbf{V}_e^p \Rightarrow i \notin \mathbf{V}_e^c \quad (23)$$

The power transmission line failure will disconnect the adjacent electric buses and alter the network topology \mathbf{G}_e^p . This subsequently necessitates the redistribution of power flow and can be mathematically represented as:

$$(i, j) \notin \mathbf{E}_e^p \Rightarrow A_{e,ij,t_f}^p = 0 \quad (24)$$

In power flow analysis, transformers are conventionally modelled as equivalent transmission line. Thus, the modelling of physical contingency at transformers adopts the same representation of the transmission line outages in (24).

4) Physical Contingency in the GS

Similarly, the physical contingency at gas source or important gas load will lead to their removal from \mathbf{G}_g^p , triggering topological reconfiguration and subsequent elimination of associated simulation boundaries. However, the physical contingency model of compressors is different from that of transformers because compressors are represented as virtual nodes in the GS rather than equivalent pipe. The reason is that natural gas can maintain continuous flow via pipe pressure gradients even during compressor failures, whereas transformers (as electromagnetic coupling devices) will completely lose energy transfer capability when compromised. Thus, physical contingency at compressors can be characterised by the change of compression ratio and be expressed as:

$$K_{cp,t_f} = 1 \quad (25)$$

For leakages along the gas pipe, the physical contingency model is determined by the leakage diameter d . As shown in Fig. 2, p_a is the atmospheric pressure and equals 0.101MPa; S_h is the leakage cross-section area, m²; $p_{leak,t}$ is the leakage pressure, Pa; $q_{leak,t}$ is the leakage flow rate, kg/s; $p_{0,t}$ is the inlet pressure of the fault pipe, kg/s. According to [24], the gas pipe leakage model can be expressed as follows.

$$q_{leak,t} = \frac{\xi S_h p_{leak,\tau}}{c} \sqrt{\frac{2\gamma}{\gamma-1} \left[\left(\frac{p_a}{p_{leak,t_f}} \right)^{\frac{2}{\gamma}} - \left(\frac{p_a}{p_{leak,t_f}} \right)^{\frac{\gamma+1}{\gamma}} \right]} \quad (26)$$

$$t \geq t_f, p_{leak,t_f} \leq p_{cr}$$

$$q_{leak,t} = \frac{\xi S_h p_{leak,\tau}}{c} \sqrt{\gamma \left(\frac{2}{\gamma+1} \right)^{\frac{\gamma+1}{\gamma-1}}} \quad t \geq t_f \quad (27)$$

$$p_{leak,t_f} > p_{cr}$$

$$p_{leak,\tau} = \begin{cases} p_{leak,t_f} & d/D \leq 0.2 \\ p_{leak,t} & d/D > 0.2 \end{cases} \quad (28)$$

$$p_{cr} = p_a \left(\frac{2}{\gamma+1} \right)^{\frac{\gamma}{\gamma-1}} \quad (29)$$

Equations (26)-(29) are the general formulas of leakage model, where γ is the adiabatic coefficient and values between 1.3-1.4; ξ is the orifice loss coefficient and values between 0.45-0.9; p_{cr} is the critical leakage pressure. For small-hole leakage with $d/D \leq 0.2$, the pipe pressure is slightly influenced by the leakage. For large-hole leakage with $d/D > 0.2$, the pipe pressure is strongly affected by the leakage and the leakage flow varies with time.

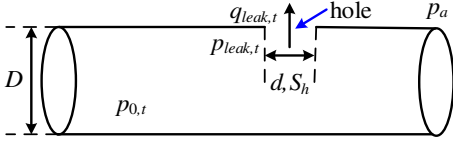


Fig. 2. Gas pipe leakage illustration as physical contingency.

IV. N-1 CONTINGENCY EVALUATION IN IEGS

A. Variable-Coefficient Analytical Method

Repeated energy flow calculation during N-1 analysis for cyber-physical IEGS faces three challenges. First, the cyber-physical interdependence leads to an extensive contingency checklist. During N-1 contingency evaluation, traversing a large number of cyber-physical contingencies imposes a substantial computational burden, making it difficult to meet real-time evaluation requirements. Second, the bidirectional coupling between the PS and GS necessitates solving a set of nonlinear PDAEs. Traditional numerical methods, such as FDM and MOC, require discretising PDEs into algebraic equations, introducing numerous redundant variables that further escalate computational complexity. Last but not least, topology reconfiguration or simulation boundary adjustments caused by contingencies can trigger abrupt or even discontinuous changes in system states. This contradicts the implicit premise of traditional numerical methods, which assume that state variables are continuously differentiable at discretised points. Such contradictions degrade the stability and accuracy of numerical methods, potentially leading to inaccurate or even infeasible N-1 contingency evaluation. The essence of these challenges stems from the dynamics and nonlinear properties inherent in (3). The former necessitates advanced numerical algorithms to ensure efficiency and

stability for contingency analysis, while the latter further amplifies this requirement.

Inspired by our previous work [21], [23], we propose a two-step approach, named variable-coefficient analytical method, to address these challenges during N-1 analysis. The first step of VC-AM adopts the philosophy of variable-coefficient transformation, converting the nonlinear PDE in (3) into a linear PDE with time-varying coefficients. This conversion ensures that the original problem maintains the stability and convergence properties of linear systems during the solution process [23]. The second step deals with the linear PDE featuring time-varying coefficients. Specifically, the linear PDE is first converted into algebraic equation based on a discretisation-free analytical method [21]. Then, the obtained solution is continuously updated until the convergence of time-varying coefficient is achieved. This step aims to resolve instability issues during contingency analysis and mitigate the complexity associated with PDE discretisation.

At the first step, we adopt the variable-coefficient (VC) method to convert that nonlinear PDE in (3) into the variable-coefficient PDE below.

$$\frac{\partial p_{x,t}}{\partial t} + \frac{c^2}{S} \frac{\partial q_{x,t}}{\partial x} = 0, \quad \frac{\partial p_{x,t}}{\partial x} + \frac{1}{S} \frac{\partial q_{x,t}}{\partial t} + \frac{\lambda |w_t| q_{x,t}}{2DS} = 0 \quad (30)$$

$$w_t \approx \frac{2c^2}{S} \frac{q_{0,t}^2 p_{L,t}^2 + q_{0,t} q_{L,t} p_{0,t} p_{L,t} + q_{L,t}^2 p_{0,t}^2}{q_{0,t} p_{0,t} p_{L,t}^2 + q_{L,t} p_{L,t} p_{0,t}^2} \quad (31)$$

where w_t is the average flow velocity along the pipe and varies with time. On this basis, solving (30)-(31) requires: **1)** initialising w_t as constant to transform (30) into linear PDEs; **2)** solving linear PDEs with constant w_t and obtain $p_{0,t}$, $q_{0,t}$, $p_{L,t}$, $q_{L,t}$; **3)** Updating w_t with (31); **4)** repeating steps above until the differences between w_t in steps **1)** and **3)** satisfy error limit.

At the second step, we adopt the analytical method (AM) to solve linear PDE with constant w_t in (30). Assuming that the set of simulation time flags is $\Gamma = \{1, 2, 3, \dots, N_t\}$ and the time interval is Δt , the analytical method transforms the gas flow equation with constant w_t into the following algebraic equations.

$$\delta_{1n,x} = \sin \frac{(2n-1)\pi x}{2L}, \delta_{2n,x} = (1-2n) \cos \frac{(2n-1)\pi x}{2L} \quad (32)$$

$$p_{x,t} = \sum_{n=1}^{\infty} \left\{ \frac{u_{n,t}}{e^{g_{n,t}}} + \frac{\lambda |w_t| F_n}{2DS} \left(q_{L,t} - \frac{q_{L,0}}{e^{g_{n,t}}} - \sum_{i=1}^j q_{L,i} \frac{e^{g_{n,i} \Delta t} - 1}{e^{g_{n,i} (t_j - t_{i-1})}} \right) \right\} \delta_{1n,x} \quad (33)$$

$$- \frac{\lambda |w_t| x}{2DS} q_{L,t} + p_{0,t}$$

$$q_{x,t} = \sum_{n=1}^{\infty} \frac{\pi DS}{\lambda |w_t| L} \left\{ \frac{u_{n,t}}{e^{g_{n,t}}} + \frac{\lambda |w_t| F_n}{2DS} \left(q_{L,t} - \frac{q_{L,0}}{e^{g_{n,t}}} - \sum_{i=1}^j q_{L,i} \frac{e^{g_{n,i} \Delta t} - 1}{e^{g_{n,i} (t_j - t_{i-1})}} \right) \right\} \delta_{2n,x} \quad (34)$$

$$+ q_{L,t}$$

where $\delta_{1n,x}$ and $\delta_{2n,x}$ are parameters defined for simplification; n is the number of Fourier components; Δt is the time step; g_n , u_n and F_n are coefficients defined for simplification, whose expressions are as follows.

$$g_{n,t} = \frac{(2n-1)^2 \pi^2 Dc^2}{2L^2 \lambda |w_t|} \quad (35)$$

$$F_n = \frac{8L(-1)^{n-1}}{(2n-1)^2 \pi^2} \quad (36)$$

$$u_{n,t} = F_n \left(K_1 + \frac{\lambda |w_t|}{2DS} q_{L,0} \right) \quad (37)$$

where K_1 is the coefficient of initial conditions for pipe pressures; $q_{L,0}$ is the initial conditions for pipe mass flow rates; K_1 and $q_{L,0}$ are given as known parameters to describe the state distribution at $t=0$.

Substituting $x=L$ and $x=0$ into (33) and (34), the pressures and mass flow rates at the pipe inlet and outlet can be linked as follows.

$$p_{L,t} = \sum_{n=1}^{\infty} e^{-g_{n,t}} u_{n,t} (-1)^{n-1} - \frac{\lambda |w_t| L}{2DS} q_{L,t} + p_{0,t} + \sum_{n=1}^{\infty} \frac{\lambda |w_t| F_n}{2DS} (-1)^{n-1} \left(q_{L,t} - \frac{q_{L,0}}{e^{g_{n,t}}} - \sum_{i=1}^j q_{L,i} \frac{e^{g_{n,t} \Delta t} - 1}{e^{g_{n,t} (j-i+1) \Delta t}} \right) \quad (38)$$

$$q_{0,t} = q_{L,t} + \frac{DS\pi}{\lambda |w_t| L} \sum_{n=1}^{\infty} (1-2n) u_{n,t} e^{-g_{n,t}} + \frac{\pi}{2L} \sum_{n=1}^{\infty} (1-2n) F_n \left(q_{L,t} - \frac{q_{L,0}}{e^{g_{n,t}}} - \sum_{i=1}^j q_{L,i} \frac{e^{g_{n,t} \Delta t} - 1}{e^{g_{n,t} (j-i+1) \Delta t}} \right) \quad (39)$$

Here, we recommend [21] for detailed derivations and explanations of (33)-(39), especially their comparisons with other numerical methods for linear PDE.

To make the analytical method for linear PDEs applicable to nonlinear PDEs, the VC-AM employs the variable-coefficient transformation. When solving (30) sequentially, we can rewrite (38)-(39) into a matrix form, as shown in (40).

$$\begin{bmatrix} p_{L,t} \\ q_{0,t} \end{bmatrix} = \begin{bmatrix} J_{1,t} & J_{2,t} \\ J_{3,t} & J_{4,t} \end{bmatrix} \begin{bmatrix} p_{0,t} \\ q_{L,t} \end{bmatrix} + \begin{bmatrix} \xi_{p,t} \\ \xi_{q,t} \end{bmatrix} \quad (40)$$

where $J_{1,t}$ - $J_{4,t}$ are the transfer matrixes at t , $\xi_{p,t}$ and $\xi_{q,t}$ are the components of p and q at t determined by initial conditions at $t=0$ and previous boundary conditions before t . Their formulations are expressed as follows.

$$J_{1,t} = 1, J_{3,t} = 0 \quad (41)$$

$$J_{2,t} = \frac{\lambda |w_t|}{2DS} \left(\sum_{n=1}^{\infty} F_n (-1)^{n-1} e^{-g_{n,t} \Delta t} - L \right) \quad (42)$$

$$J_{4,t} = \frac{\pi}{2L} \sum_{n=1}^{\infty} F_n (1-2n) e^{-g_{n,t} \Delta t} + 1 \quad (43)$$

$$\xi_{p,t} = \begin{cases} \gamma_{p,t} & t=1 \\ \gamma_{p,t} + \sum_{k=1}^{t-1} J_{2,t-k} q_{L,t-k} & t>1 \end{cases} \quad k \in \Gamma \quad (44)$$

$$\xi_{q,t} = \begin{cases} \gamma_{q,t} & t=1 \\ \gamma_{q,t} + \sum_{k=1}^{t-1} J_{4,t-k} q_{L,t-k} & t>1 \end{cases} \quad k \in \Gamma \quad (45)$$

$$\gamma_{p,t} = \gamma_{p,t-1} + \sum_{n=1}^{\infty} F_n K_1 (-1)^{n-1} e^{-g_{n,t}} (e^{g_{n,t} \Delta t} - 1) \quad (46)$$

$$\gamma_{q,t} = \gamma_{q,t-1} + \frac{DS\pi}{\lambda |w_t| L} \sum_{n=1}^{\infty} (1-2n) F_n K_1 e^{-g_{n,t}} (e^{g_{n,t} \Delta t} - 1) \quad (47)$$

where $\gamma_{p,t}$ and $\gamma_{q,t}$ are the components of p and q at t determined by initial conditions at $t=0$. The flowchart of gas flow calculation with VC-AM is summarised in TABLE II.

TABLE II
FLOW CHART OF VC-AM FOR ENERGY FLOW CALCULATION OF GS

| |
|--|
| Input system topology, boundary conditions, and error limit ϵ |
| Input state distribution at $t-1$ and set $w_{init}=w_{t-1}$ |
| If contingency occurs at t |
| If gas pipe contingency |
| Reformulate boundary conditions according to (26)-(29). |
| Adjust system topology and network equations. |
| Else |
| Reformulate boundary conditions according to Section III.B. |
| End |
| End |
| While $ w_{init}-w_t \leq \epsilon$ |
| Substitute w_{init} into (35)-(47) to obtain $g_{n,t}$, $u_{n,t}$, $\xi_{p,t}$, $\xi_{q,t}$, $\gamma_{p,t}$ and $\gamma_{q,t}$. |
| Substitute w_{init} into (41)-(43) to obtain $J_{1,t}$ - $J_{4,t}$. |
| Solve (38)-(39) to obtain $q_{0,t}$ and $p_{L,t}$. |
| Substitute $q_{0,t}$, $p_{L,t}$, $p_{0,t}$ and $q_{L,t}$ into (31) to obtain w_t . |
| Set $w_{init}=w_t$. |
| End |

B. Discussions on the VC-AM

Here, we present some important properties on the implementation of the VC-AM in N-1 analysis.

1) Proof of Reasonable Simplifications

In VC-AM, gas states are expressed a finite combination of Fourier components. Related variables include $\delta_{1,n}$, $\delta_{2,n}$, g_n , F_n and u_n , which ultimately manifest in J_2 and J_4 . Thus, it is necessary to simplify these equations into a truncated Fourier series representation because retaining all component will become computationally intractable.

Substituting $\delta_{1,n}$, $\delta_{2,n}$, g_n , F_n and u_n into J_2 and J_4 , we have:

$$\begin{cases} J_{2,t} = \frac{4\lambda |w_t| L}{DS\pi^2} \left(\sum_{n=1}^{\infty} \frac{e^{-k(2n-1)^2}}{(2n-1)^2} - L \right) \\ J_{4,t} = 1 + 4\pi \sum_{n=1}^{\infty} \frac{(-1)^{n-1}}{(1-2n)\pi^2} e^{-k(2n-1)^2} \\ k = \frac{\pi^2 Dc^2}{2L^2 \lambda |w_t|} \Delta t, k > 0 \end{cases} \quad (48)$$

According to (48), the Fourier component terms involved in J_2 and J_4 include $1-2n$, $(-1)^{n-1}$, $\exp(-k(2n-1)^2)$ and can be summarised as follows.

$$\begin{cases} f_1(n) = \sum_{n=1}^{\infty} \frac{e^{-k(2n-1)^2}}{(2n-1)^2}, & \lim_{n \rightarrow \infty} f_1(n) = 0 \\ f_2(n) = \sum_{n=1}^{\infty} \frac{(-1)^{n-1}}{(1-2n)\pi^2} e^{-k(2n-1)^2}, & \lim_{n \rightarrow \infty} f_2(n) = 0 \end{cases} \quad (49)$$

Therefore, as n increases, these Fourier component terms rapidly approach zero at an extremely fast rate. Given $k > 0$, for J_2 , the denominator terms of its Fourier components grow quadratically with n , while the numerator terms decay exponentially toward zero. As a result, the Fourier component terms in J_2 vanish at a super-exponential rate. Similarly, for J_4 , the denominator terms of its Fourier components grow linearly with n , whereas the numerator terms also decay exponentially toward zero. Hence, the Fourier component terms in J_4 likewise vanish at a super-exponential rate.

Next, we analyse the value range of k . For typical GS, L generally ranges from tens of kilometres to several kilometres, resulting in L^2 on the order of 10^6 to 10^8 , λ is on the order of 10^{-2} to 10^{-1} , w is on the order of 10^0 to 10^1 , $\pi^2 D$ is on the order of 10^0 , and c^2 is on the order of 10^5 . In typical application scenarios (e.g., economic dispatch or N-1 evaluation in this paper), Δt is on the order of 10^1 to 10^2 . Consequently, k falls within the range of 10^{-2} to 10^0 . Considering an extreme case of $k=0.01$, Fourier-related components in (48) will become sufficiently small to be negligible when n approximates 10. Furthermore, since k is typically greater than 0.01 in practical scenarios, they decay to zero at an even faster rate. Thus, in general cases, the truncated Fourier components no longer affect the accuracy of VC-AM when $n=10$.

2) Methodology Differences

The proposed VC-AM has distinct differences from our previous work. Firstly, the variable-coefficient method in [23] and analytical method in [21] are designed for GS with fixed flow directions under normal conditions. However, topology reconfiguration caused by contingencies may lead to flow reversal, rendering the original variable-coefficient method inapplicable, whereas the proposed VC-AM can effectively resolve this reversal flow problem. Secondly, in previous variable-coefficient method, the iterative updating of average flow velocity still relies on FDM, which inherently suffers from computational complexity and numerical oscillations of discretisation-based approaches. Thirdly, the analytical method in [21] targets linear networks, wherein the related parameters like w , g_n , F_n , u_n , J_2 and J_4 are time-invariant. Such a linear network is unsuitable for contingency analysis because it assumes the average flow velocity to be constant. In contrast, VC-AM overcomes this simplification and addresses nonlinear networks with time-varying average flow velocity. Fourthly, analytical method and VC-AM also differ in their computational mechanisms. The former method for simulation is a one-time computational process as the parameters can be determined offline, while the latter requires more advanced iterative updates and performs calculations in a moment-by-moment manner.

3) Impact of Fault Locations

Different from the static N-1 analysis in the PS, the gas pipe leakage locations in the GS determine the dynamic fault impact

in IEGS. Traditional numerical methods suffer from this issue for two reasons. First, numerical methods require spatial discretisation along the pipe. Suitable pipe segments are required to ensure the accuracy and numerical stability, hindering the efficiency for online N-1 analysis. Second, the fault location may not be an integer multiple of the spatial step sizes Δx , introducing additional errors. In contrast, in analytical methods, state distribution along the pipe are functions of x . For different fault locations, one only needs to substitute x into (33) and (34) to obtain leakage information, thereby avoiding the aforementioned issues.

C. Performance Indexes for N-1 Contingency Evaluation

The N-1 contingency evaluation in the IEGS is different from that in the PS because the CPCs may affect the system performance gradually with its impact propagation due to gas flow dynamics. Thus, the evaluation result of IEGS is time-dependent at each time step while that of the PS is time-independent. To evaluate the impact of contingencies in the whole simulation period, the PIs in the PS [25] are extended into the IEGS for N-1 analysis.

The PIs in the PS at arbitrary τ are:

$$\begin{aligned} \text{PI}_{e,\tau} &= \text{PI}_{e,U,\tau} + \text{PI}_{e,S,\tau} + \text{PI}_{e,G,\tau} \\ &= \sum_t \left(\sum_i \left(\frac{U_{i,t} - U_{i,\text{rate}}}{\Delta U_{i,\text{max}}} \right)^2 + \sum_k \left(\frac{P_{l,k,t}^2 + Q_{l,k,t}^2}{S_{l,k,\text{max}}^2} \right)^2 \right) \\ &\quad + \sum_t \sum_i \left(\frac{P_{Gi,t}}{P_{Gi,\text{max}}} \right)^2 \quad \begin{matrix} t \geq \tau \\ t, \tau \in \Gamma \end{matrix} \end{aligned} \quad (50)$$

where PI_e , $\text{PI}_{e,U}$, $\text{PI}_{e,S}$ and $\text{PI}_{e,G}$ are the PIs of the whole PS, the voltage amplitude, line power flow, and generator capacity, respectively; U_{rate} is the rated voltage amplitude; $S_{l,\text{max}}$ is the line power flow capacity; ΔU_{max} is the permitted voltage amplitude deviation.

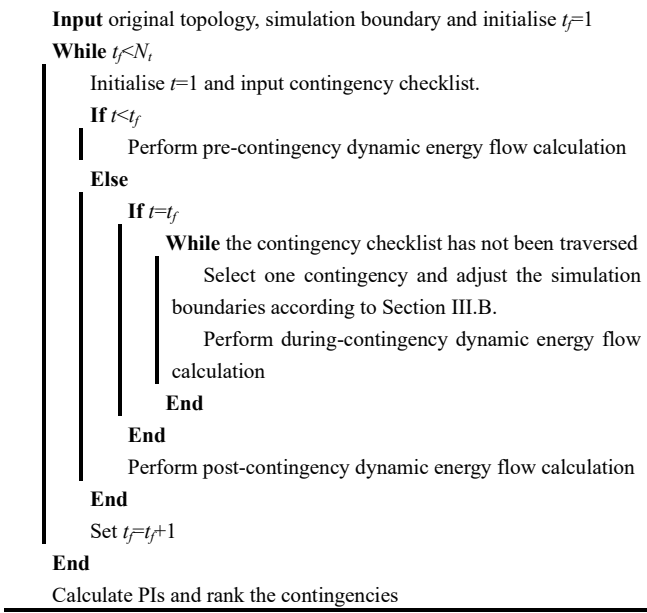
The PIs in the GS at arbitrary τ are:

$$\begin{aligned} \text{PI}_{g,\tau} &= \text{PI}_{g,p,\tau} + \text{PI}_{g,q,\tau} \\ &= \sum_t \left(\sum_i \left(\frac{p_{nd,i,\tau} - p_{nd,i,\text{rate}}}{\Delta p_{nd,i,\text{max}}} \right)^2 + \sum_i \left(\frac{q_{nd,i,\tau}}{q_{i,nd,\text{max}}} \right)^2 \right) \quad \begin{matrix} t \geq \tau \\ t, \tau \in \Gamma \end{matrix} \end{aligned} \quad (51)$$

where PI_g , $\text{PI}_{g,p}$, and $\text{PI}_{g,q}$ are the PIs of the whole GS, node pressure, and node mass flow rate, respectively; $q_{nd,\text{max}}$ is the maximum node mass flow rate; $p_{nd,\text{rate}}$ is the rated node pressure; $\Delta p_{nd,\text{max}}$ is the permitted node pressure deviation. The procedure of the N-1 contingency evaluation for cyber-physical IEGS is summarised in TABLE III.

It should be noted that multiple PI in (50) and (51) are designed to quantify the overall impact of a contingency on the system. In traditional N-1 contingency evaluations in the PS, equal weights are typically assigned to each sub-index. When these weights conflict, energy system operators can adjust the weights of different indices based on their preferences to generate prioritised contingency rankings.

TABLE III
FLOW CHART OF N-1 ANALYSIS IN CYBER-PHYSICAL IEGS



V. CASE STUDY

The section outlines three aspects to assess the efficacy of the proposed N-1 contingency evaluation method on cyber-physical IEGS. Case I evaluates the performance of VC-AM within a single GS pipe across various settings. Case II serves as a demonstrative case to illustrate the impact of diverse CPCs, involving a 6-bus PS connected to a 4-node GS via one GT and P2G. In Case II, B1 is the slack bus, B2 is the autonomous PV bus and B6 is the communication-dependent PV bus. Case III is for N-1 contingency evaluation, including a modified IEEE 30-bus PS interfaced with a 27-node GS. The configurations of the cyber-physical IEGS as two test systems are depicted in Fig. 3 and detailed data is available in [26].

For clarity of presentation, the diagram of Case II does not explicitly depict the coupling relationships between physical and cyber nodes, though their connectivity is implicitly defined by the one-to-one interdependence in their numbering. For generators in Case II, B1 is the slack bus, B2 and B13 are the autonomous PV buses, and the others are communication-dependent PV buses. As for the gas sources, N20 is the communication-dependent source node. The communication nodes 4, 8, 9, 10, 13, 14, 21, 22, 26, 27 of the GS are powered by electric buses 2, 22, 27, 8, 23, 10, 12, 14, 15, 16, 17, 18, respectively. The PS and GS are interconnected via three GTs and one P2G situated at electric buses 2, 27, 23, 8, and gas nodes 13, 21, 26, 24. Five methods are used for comparison, including, the Euler Implicit Scheme (EIS) in [18], the MOC in [19], the AM in [21], the VCM in [23] and the Central Implicit Scheme (CIS) in [27]. MOC with sufficiently small step sizes is used as reference due to its excellent numerical performance. Simulations were executed on a laptop with an Intel i9 CPU and 16GB of RAM, using Matlab 2022a for coding. The mean relative difference (MRD) and the largest relative difference (LRD) are employed for performance evaluation.

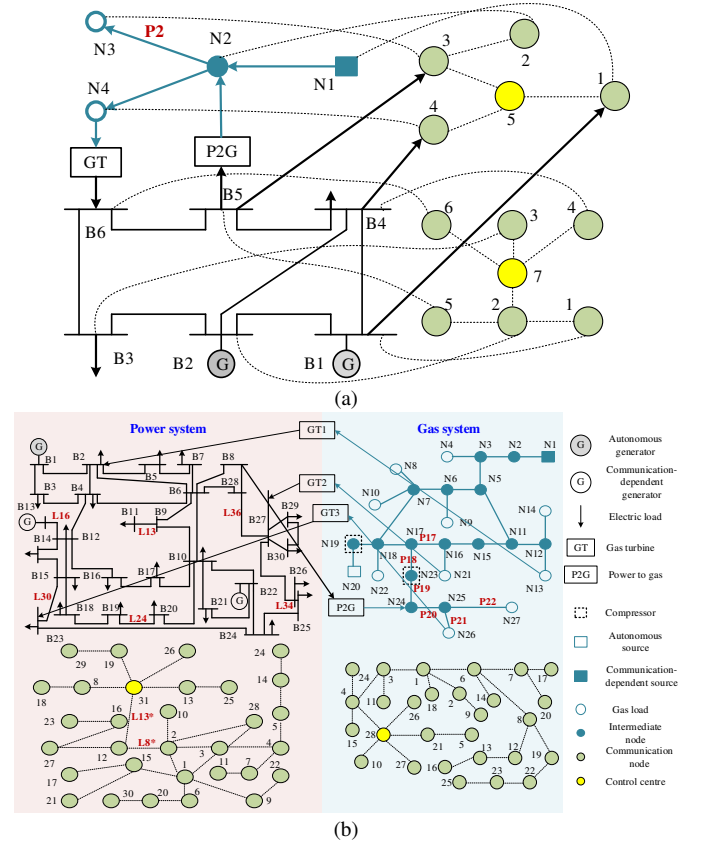


Fig. 3. Test systems of cyber-physical IEGS in case study: (a) Case II; (b) Case III.

A. Verification of VC-AM in Contingency Analysis

We choose the pipe with $D=0.4\text{m}$, $L=50\text{km}$, $\lambda=0.03$ for illustration. The results are summarised in Fig. 4 and TABLE V. It should be noted that Δt in MOC is much smaller than the other methods due to its strict stability constraints.

1) Normal Operation

Fig. 4(a)-(b) shows the simulation results of node mass flow rate over a 12-hour duration under normal operation, where six methods exhibit similar trajectories. Using MOC as the reference, the MRDs of different methods remain below 1.5% in Fig. 4(a), and scale proportionally with step sizes in Fig. 4(b). Since the analytical method represents the ideal solution for numerical methods with infinitesimal steps, VC-AM demonstrates the closest approximation to MOC, followed by AM which neglects gas flow nonlinearity. In this scenario, AM proves to be the most computationally efficient due to its linear characteristics, with VC-AM, EIS, VC, and CIS following in descending order of efficiency. MOC remains the most complex method as it requires significantly smaller step sizes to maintain stability.

2) Small-Hole Leakage

We set $\Delta x=500\text{m}$, $\Delta t=1\text{min}$ for CIS, EIS and VC, and $\Delta x=500\text{m}$, $\Delta t=1\text{s}$ for MOC. Fig. 4(c)-(d) present the results of node mass flow rate under different small-hole leakages. Similar to those in normal operation, the results of VC-AM approximate the MOC more closely than the other methods, with much smaller MRDs in both scenarios. The key distinction lies that VC fails to converge under these scenarios, as the method is primarily designed for normal operation. Under fault

conditions, numerical oscillations and discontinuous boundaries prevent the discretisation-based iterative scheme from converging to a feasible solution. A similar issue arises with AM, which exhibits significant errors in TABLE V. When a gas pipe leakage occurs, the sudden shift in system operating state forces AM to adjust pressure and flow rates aggressively to maintain constant gas velocity, resulting in substantial deviations from the true solution. As for the efficiency, VC-AM maintains its superiority and takes around 0.3s to finish the simulation. In contrast, discretisation-based methods demand longer computation times by an order of magnitude.

3) Large-Hole Leakage

With the same settings of leakage diameter and fault time in large-hole leakage, the leakage flow rate simulation results are compared with six methods. In this condition, VC-AM and AM converges despite different fault settings, while the other four methods diverge at the fault time despite different step sizes, as shown in Fig. 4(e). In this scenario, AM exhibits greater deviation from the true solution. This occurs because the flow velocity changes more dramatically during large-hole leakage faults. To maintain constant gas flow velocity, AM must reduce the pressure difference between the pipe inlet and leakage point, resulting in overestimated leakage pressure. Since leakage flow rate scales with the leakage pressure, this effect further amplifies the overall error. Fig. 4(f) shows the iterative processes of four discretisation-based methods. Their divergence is mainly caused by the discontinuity of simulation boundaries. The simulation boundary at leakage points is the fixed leakage flow under small-hole leakage, while that under large-hole leakage is the time-varying equation in (26)-(27). Since the smoothness and continuity are fundamental conditions that ensure the effectiveness of the numerical methods, the non-convergence is expected.

4) Arbitrary Contingency

We refine the simulation boundaries and incorporate randomness into fault location x , leakage diameter d and fault time t_f . The fault location x , leakage diameter d and fault time t_f are assumed to follow uniform distributions, where $x \sim \mathcal{U}(0, 50\text{km})$ with a mean of 25km and a variance of $(50\text{km})^2/12$, $d \sim \mathcal{U}(0, 0.38\text{m})$ with a mean of 0.19m and a variance of $(0.38\text{m})^2/12$, and $t_f \sim \mathcal{U}(0, 12\text{h})$ with a mean of 6h and a variance of $(12\text{h})^2/12$. Then, we utilise an independent and identically distributed sampling approach to generate 1000 random datasets, as shown in Fig. 4(g). The datasets are provided by the authors and accessible online in [28].

The simulation results demonstrate significant differences in convergence performance among the investigated methods. The AM achieves 100% convergence rate, benefiting from its linear formulation that eliminates iterative computations and associated convergence challenges. However, this comes at the cost of reduced accuracy. The VC-AM closely follows with a 99.7% convergence rate, with the three exceptional cases. The non-convergence is attributable to unreasonable parameter settings because excessive leakage diameters can induce negative pressure at leakage points. This essentially confirms VC-AM's inherent potential for 100% convergence under proper parameterisation. In contrast, discretisation-based methods, like EIS, CIS, MOC and VC, exhibit significant non-

convergence rates, particularly in large-hole leakage scenarios, which aligns with our prior analysis. While these numerical approaches maintain acceptable convergence performance for small-hole leakage simulations, they suffer from significantly lower computational efficiency compared to VC-AM, as summarised in TABLE VI.

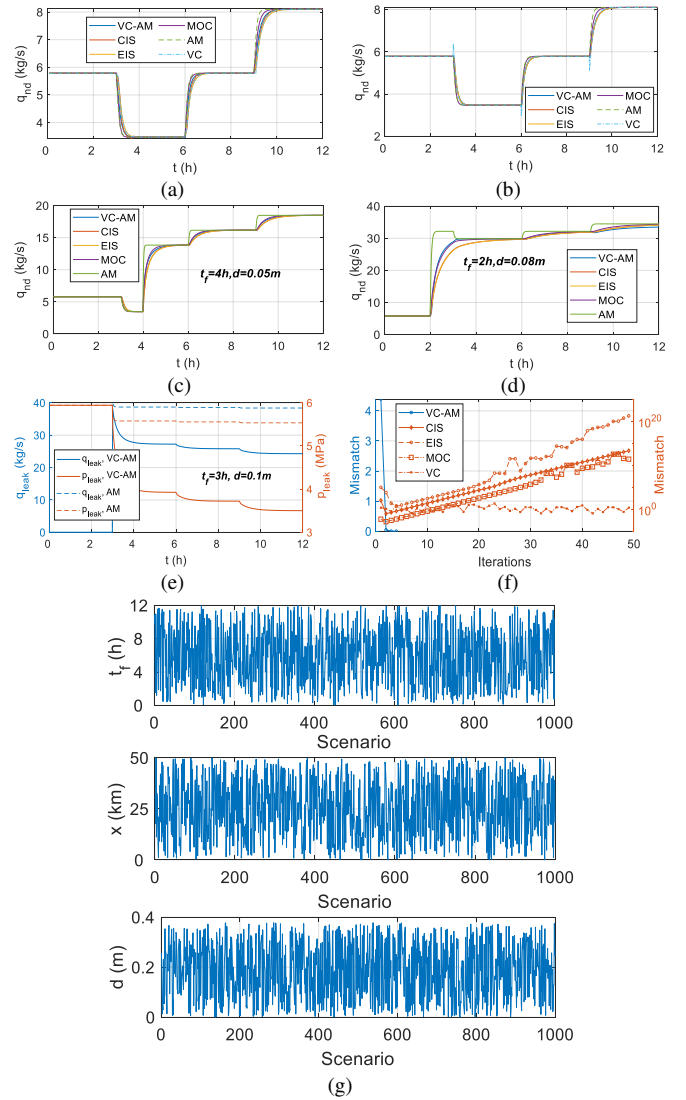


Fig. 4. Contingency simulation: (a) Normal operation with $\Delta x=5\text{km}$, $\Delta t=5\text{min}$ for EIS and CIS, 10s for MOC; (b) Normal operation with $\Delta x=500\text{m}$, $\Delta t=1\text{min}$ for EIS and CIS, 1s for MOC; (c) Small-hole leakage at $x=25\text{km}$; (d) Small-hole leakage at $x=37.5\text{km}$; (e) Large-hole leakage at $x=37.5\text{km}$ by VC-AM; (f) Iterative process at fault time; (g) 1000 random generated settings.

TABLE V. SIMULATION RESULTS IN CASE I

| Scenario | | (a) | (b) | (c) | (d) | (e) |
|-----------------|-------|-------|--------|--------|--------|-------|
| MRD/% | VC-AM | 0.58 | 0.46 | 0.66 | 1.22 | — |
| | CIS | 1.25 | 0.75 | 1.31 | 2.27 | N/A |
| | EIS | 1.30 | 0.77 | 1.33 | 2.32 | N/A |
| | AM | 1.26 | 0.76 | 1.93 | 5.30 | — |
| | VC | 1.30 | 0.77 | N/A | N/A | N/A |
| | MOC | — | — | — | — | N/A |
| Solution time/s | VC-AM | 0.011 | 0.190 | 0.380 | 0.321 | 0.325 |
| | CIS | 0.040 | 0.710 | 0.794 | 0.862 | N/A |
| | EIS | 0.014 | 0.980 | 1.083 | 1.235 | N/A |
| | AM | 0.006 | 0.014 | 0.018 | 0.016 | 0.031 |
| | VC | 0.036 | 0.847 | N/A | N/A | N/A |
| | MOC | 0.242 | 40.248 | 46.714 | 47.741 | N/A |

N/A refers to non-convergence

TABLE VI Extensive SIMULATIONS IN CASE I

| | VC-AM | CIS | EIS | AM | VC | MOC |
|--------------------|-------|------|------|------|------|------|
| Convergence rate/% | 99.7 | 70.5 | 73.2 | 100 | 23.7 | 75.5 |
| Solution time/s | 0.34 | 0.92 | 1.31 | 0.02 | 0.96 | 44.5 |

B. Impact of Cyber-Physical Contingencies

This part designs several cyber-physical contingency scenarios to investigate impact of CPCs in Case II. During simulation, we set $\Delta x=500\text{m}$, $\Delta t=5\text{min}$ for CIS, EIS and VC, and $\Delta x=500\text{m}$, $\Delta t=1\text{s}$ for MOC. The results are summarised in TABLE VII and Fig. 5.

(1) **S1**: A physical contingency at B5 of the PS is initiated at 3h. This contingency not only leads to the disconnection of the electric load and P2G but also causes the communication node at N3 in the GS to lose its control capability. This contingency propagation from physical to cyber layer results in the constant node pressure from that point onward. The distribution of mass flow rates is further changed due to its coupling with pressure in PDE, as shown in Fig. 5(a)-(b).

(2) **S2**: A cyber contingency emerges at B6 at 6h, leading to complex propagation. On one front, B6 loses its voltage control and becomes an equivalent PQ bus with predefined active and reactive power injections, which may potentially drive voltage U_6 beyond limits. Simultaneously, the coupled GT alters its operational behaviour and impacts the gas flow consumption at N3. In response to this contingency, the gas source at N1 subsequently adjusts its output gas flow rate, along with a noticeable time lag, as depicted in Fig. 5(c).

(3) **S3**: A significant leakage occurs at the 15km along Pipe 2 at 4h. Consequently, the pressure distribution downstream of the leakage undergoes a precipitous decline, prompting a reallocation of gas states since then. As illustrated in Fig. 5(d)-(e), the pressure during the contingency plummets below a critical value. This situation is likely to trigger a GT shutdown, causing a power outage and culminating in a cascading failure.

(4) **S4**: A physical contingency at B4 of the PS is detected at 3h. The sudden load loss initially results in a voltage increase at B4, which in turn causes the communication node at N4 to lose control. Consequently, N4 in the GS maintains a constant gas load profile. This disruption subsequently impacts the GT output at B6, redistributing the power flow and impacting the voltage profile at U6, which consequently initiates a bidirectional contingency propagation, as shown in Fig. 5(f).

(5) **S5**: A cyber contingency occurs at the communication node 3 of GS at 2h, triggering a cyber-cyber contingency that disconnects communication node 2 from the CC. This disruption not only changes the gas load profile at N3 and N2, but also affects the electric load profile at B6, as shown in Fig. 5(g)-(h).

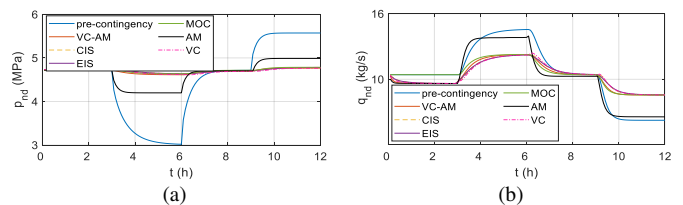
TABLE VII benchmarks the performance of various methods across five scenarios. Although numerical methods show non-convergence in S3, the proposed VC-AM achieves convergence in all scenarios. While convergence is attained, VC-AM exhibits a marked efficiency advantage, being more than five times quicker than EIS, CIS and VC, and over a hundred times faster than MOC. This superiority stems from two primary factors. Firstly, VC-AM bypasses PDE

discretisation, thus eliminating unnecessary equations during iterative calculations. In contrast, for CIS, EIS and VC, a Δx of 500 introduces over 220 redundant equations per time step compared to VC-AM. For MOC, the situation is even more complex; its stability requires sufficiently-small time steps, with $\Delta t=1\text{s}$ further increasing the computational demand by a factor of sixty. This renders MOC impractical for real-time applications. Secondly, VC-AM typically converges within an average of four iterations, whereas other methods are relatively slower to converge. As depicted in Fig. 5(i), in S2, VC-AM primarily converges in three iterations, whereas CIS, EIS and VC converged after five, six and twelve iterations. Thus, the high efficiency of VC-AM is evident.

Regarding accuracy, VC-AM closely approximates the small step-size MOC in most scenarios, outperforming EIC, CIS and VC, while AM performs worst. As detailed in [21], the analytical method bypasses approximation errors and can be considered the ideal solution for numerical methods with infinitesimally small step sizes. When extended to nonlinear PDEs, this advantage is maintained, and the nonlinearity is effectively managed through variable-coefficient iterations. This capability is crucial for contingency simulations that involve strong nonlinearity and discontinuity, ensuring that VC-AM provides a more accurate representation of the system's behaviour under such complex conditions. Correspondingly, although AM adopts a similar philosophy, its linear characteristics result in solutions that deviate significantly from those obtained by nonlinear methods, with maximum MRD and LRD reaching as high as 8.08% and 41.1%, respectively. Therefore, even though AM achieves the fastest convergence across all scenarios, its accuracy remains unacceptable. Meanwhile, the limitations of VC resemble those of EIS and CIS, since it fundamentally relies on PDE discretisation.

TABLE VII
SIMULATION COMPARISONS WITH FIVE CYBER-PHYSICAL CONTINGENCY SCENARIOS IN CASE II

| Scenario | | S1 | S2 | S3 | S4 | S5 |
|-----------------|-------|------|------|------|------|------|
| MRD/% | VC-AM | 0.87 | 2.41 | — | 2.39 | 0.22 |
| | CIS | 1.08 | 2.99 | N/A | 2.35 | 0.44 |
| | EIS | 1.09 | 2.39 | N/A | 2.29 | 0.45 |
| | AM | 5.09 | 8.08 | — | 2.92 | 3.03 |
| | VC | 1.17 | 2.78 | N/A | 1.53 | 0.49 |
| | MOC | — | — | N/A | — | — |
| LRD/% | VC-AM | 7.71 | 11.1 | — | 11.5 | 3.77 |
| | CIS | 7.69 | 13.5 | N/A | 11.7 | 7.58 |
| | EIS | 7.96 | 12.7 | N/A | 10.8 | 7.52 |
| | AM | 23.7 | 41.1 | — | 33.0 | 36.1 |
| | VC | 7.70 | 13.6 | N/A | 11.4 | 7.61 |
| | MOC | — | — | N/A | — | — |
| Solution time/s | VC-AM | 0.31 | 0.34 | 0.62 | 0.29 | 0.32 |
| | CIS | 1.20 | 5.43 | N/A | 1.36 | 5.33 |
| | EIS | 1.68 | 2.86 | N/A | 1.76 | 2.01 |
| | AM | 0.30 | 0.27 | 0.28 | 0.28 | 0.30 |
| | VC | 3.77 | 3.05 | N/A | 4.58 | 8.23 |
| | MOC | 230 | 248 | N/A | 241 | 289 |



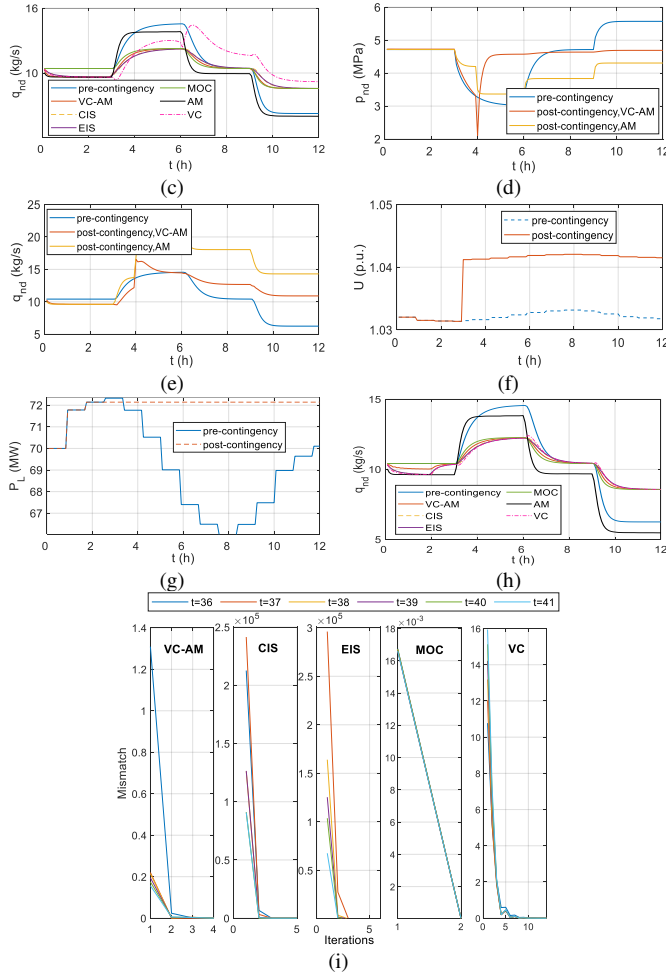


Fig. 5. Contingency simulation: (a) $p_{nd,3}$ in S1; (b) $q_{nd,1}$ in S1; (c) $q_{nd,1}$ in S2; (d) $q_{nd,1}$ in S3; (e) $p_{nd,3}$ in S3; (f) U_6 in S4; (g) $P_{L,5}$ in S5; (h) $q_{nd,1}$ in S5; (i) Iterative process in S2 during a specific period.

C. N-1 Contingency Evaluation

This section studies the proposed N-1 contingency evaluation method, with an assessment period spanning 12 hours and employing a time interval of 15 min. We set $\Delta x=1000\text{m}$ for CIS and $\Delta x=450\text{m}$ for EIS because EIS fails to converge with $\Delta x=500\text{m}$ and $\Delta x=1000\text{m}$. This adjustment significantly increases the computational demand for EIS. The iterative error limit is 10^{-3} and the maximum iteration number is 250 for all the methods. A leakage diameter of 0.1m is specified to encompass evaluations for both small-hole and large-hole gas pipe leakage within this scenario. At each time step, 241 contingencies are checked. The convergence rate, defined as the proportion of contingencies that achieve convergence serves as a key metric for method comparisons.

Fig. 6(a)-(b) illustrates the solution time for N-1 contingency evaluation at each time step, demonstrating a general trend of decreasing computational duration. Given that the CPCs within the IEGS at any given time influence the security of subsequent periods due to gas flow dynamics, earlier occurrences of CPCs necessitate longer evaluation periods and greater computational complexity. Among the six methods, the MOC proves unsuitable due to prohibitive computational costs. In Case III, stability constraints require $\Delta t \leq 2\text{s}$ for MOC implementation, resulting in computation time exceeding three hours per

contingency scenario. This renders the methodology infeasible for comprehensive contingency checklist evaluation within operational time constraints. VC also demonstrates limited practicality in this application as it exhibits divergence across all test scenarios. This limitation stems fundamentally from VC's inherent reliance on fixed flow directions. We observe that gas load fluctuations induce dynamic flow direction starting at $t=30\text{min}$ under normal operations, with such directional change becoming particularly pronounced under contingency conditions. These directly violate VC's foundational premises, thereby explaining its failed convergence. Among the four feasible methods, EIS has the longest solution time, followed by CIS and VC-AM, while AM is the fastest. This is because EIS only converges at $\Delta x=450\text{m}$, resulting in a larger problem scale than CIS. Additionally, EIS exhibits slower iterative convergence, with its N-1 contingency evaluation at the initial stage even exceeding 10^4s . Although CIS also faces discretisation challenges, its larger Δx leads to a relatively smaller problem scale, improving computational efficiency by several times compared to EIS. VC-AM achieves an order-of-magnitude reduction in computational time over EIS and CIS, as it avoids redundant discretisation, keeping the problem scale much smaller than traditional numerical methods. The solution time at each time step remains under 300s. Meanwhile, AM further enhances efficiency by leveraging its linear characteristics, eliminating the need for excessive iterations.

Fig. 6(b) depicts the convergence rate across all time steps. The average convergence rates are as follows. EIS achieves the lowest rate at 77.4%, followed by CIS at 94.8% and VC-AM at 95.9%, with AM leading at 97.9%. Non-convergence can be attributed to three primary factors: (1) inherently unsolvable scenarios; (2) numerical issues arising from inappropriate step sizes or abrupt boundary conditions; and (3) inadequate initial estimates or iteration limits.

Theoretically, AM should not face convergence issues. However, it fails to converge when N-1 contingencies on either transmission lines 13, 24, 16, or bus B27 fails. Notably, the contingency at B27 even triggers non-convergence from GS side. Similar convergence failures are observed in VC-AM, EIS, and CIS. Beyond power system contingencies, gas system contingencies also exhibit comparable effects. For instance, when large-hole leakages occur in pipes 19, 20 and 21, VC-AM, EIS and CIS all diverge due to negative pressures. In contrast, AM optimistically evaluates the contingency impact, failing to accurately capture this and revealing inaccuracies in its N-1 contingency evaluation results. Specifically, CIS and EIS fail to converge under large-hole leakages with low pressures, whereas VC-AM demonstrates superior robustness. Regarding numerical issues, step size adjustments can improve feasibility to some extent. For example, reducing EIS's Δx from 500m or 1000m to 450m enhances convergence, though at the cost of drastically computational demand. In some cases, a single time-step solution in EIS may require hours, rendering this approach impractical for large-scale studies. Increasing the permitted number of iterations does not resolve non-convergence in EIS and CIS but enhances the convergence rate of VC-AM, as shown in Fig. 6(c)-(e). When the iteration limit is raised to 2000,

the average convergence rate of VC-AM improves to 96.4%. These results highlight VC-AM's superior reliability in ensuring feasible N-1 contingency evaluation.

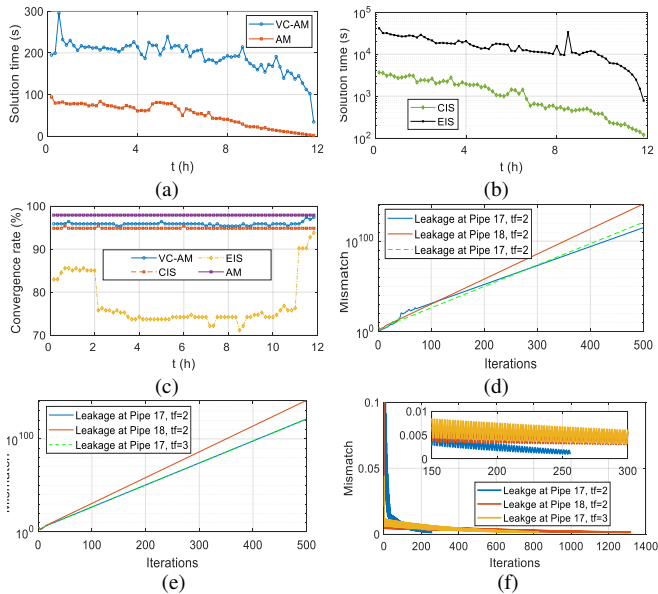


Fig. 6. N-1 contingency simulation: (a) Solution time of VC-AM and AM; (b) Solution time of CIS and EIS; (c) Convergence rate; (d) Iterative process of EIS; (e) Iterative process of EIS; (f) Iterative process of VC-AM.

TABLE IX outlines the top 10 impactful contingencies. The varying rankings observed at different time steps underscore the importance of integrating energy flow dynamics into N-1 contingency evaluation. At fault time $t_f=6h$, VC-AM, CIS and EIS yield highly consistent rankings, while AM exhibit significant deviations. As previously discussed in Fig. 4, AM's evaluation of GS contingencies proves overly optimistic as they barely induce noticeable state deviations. Consequently, its checklist predominantly ranks PS contingencies as the highest impact, rendering these results unreliable. Conversely, EIS and CIS frequently encounter non-convergence due to negative gas pressure, exaggerating leakage impact evaluations. This explains why the differences between CIS, EIS and VC-AM primarily occurs in the 8th and 9th ranked contingencies. The results at $t_f=12h$ reveals analogous rankings because EIS and CIS systematically overestimate leakage impact, while AM remains unrealistically optimistic about GS contingencies.

According to TABLE IX, CPCs consistently rank higher compared to purely physical or cyber contingencies. This stems from the cyber-physical interdependence that amplify both the failure scope and severity. For instance, the outage of B27 not only redistributes power flow and reduces gas load at N21 but also disrupts the communication node linked to N9. Cyber branch contingency at L13 critically impair control command deliverability and disconnects communication links to over 10 buses, which subsequently compromises GS operation.

We further adjusted the weights of different sub-indices, and the results show that while the weights significantly influence the overall ranking, their impact on the ordering of top-risk contingencies is negligible. As all sub-indices have been standardised, the variations in PS values caused by contingency-induced state deviations far outweigh the effects of weight adjustments within the normal range. Consequently,

when the weights of sub-indices are modified, the rankings of less critical contingencies (those not associated with major risks) exhibit noticeable changes, whereas the top-ranked contingencies remain almost unchanged.

TABLE IX
CONTINGENCY RANKING AT DIFFERENT FAULT TIME

| Rank | $t_f=6h$ | | | | $t_f=12h$ | | | |
|------|----------|-----|-----|------|-----------|-----|-----|------|
| | VC-AM | CIS | EIS | AM | VC-AM | CIS | EIS | AM |
| 1 | B27 | B27 | B27 | B27 | B27 | B27 | B27 | B27 |
| 2 | P22 | P22 | P22 | L34 | P22 | P22 | P22 | L34 |
| 3 | L34 | L34 | L34 | L16 | L34 | L34 | L34 | L16 |
| 4 | L16 | L16 | L16 | L13 | L16 | L16 | L16 | L13 |
| 5 | P21 | P21 | P21 | L13* | L13* | P21 | P21 | L13* |
| 6 | P20 | P20 | P20 | B22 | B22 | P20 | P20 | B22 |
| 7 | P19 | P19 | P19 | L36 | L36 | P19 | P19 | L36 |
| 8 | L13 | L13 | L13 | L8* | B2* | L13 | L13 | L8* |
| 9 | L13* | P18 | P18 | B2* | L8* | P18 | P18 | B2* |
| 10 | B22 | P17 | P17 | B1* | P20 | P17 | P17 | L30 |

B* refers to the communication node, L* refers to the communication link

V. CONCLUSIONS

The paper introduces an N-1 contingency evaluation method for cyber-physical IEGS. By modelling various CPCs as reformulations of simulation boundaries, a VC-AM is devised to address scenarios characterised by discontinuity and abrupt changes. Case studies reveal several key insights.

(1) Cyber-physical interdependence broadens the scope and severity of failure impacts. Thus, CPCs commonly rank higher than purely cyber or physical failures in the contingency checklist, particularly for highly interconnected nodes within the IEGS. Cyber-physical interdependence amplifies the failure severity, making CPCs rank higher in the contingency checklist than purely cyber or physical failures. This prioritisation is particularly pronounced for critical nodes with higher cyber-physical interdependence.

(2) Traditional discretisation-based methods struggle with real-time N-1 contingency evaluation due to their high computational complexity and potential convergence problems. In contrast, the VC-AM achieves acceptable accuracy across diverse cyber and physical contingency scenarios while delivering a several-fold improvement in computational efficiency and demonstrating an over 95% convergence rate.

While VC-AM achieves notable efficiency enhancements, its application to long-term N-1 contingency evaluation in large-scale IEGS faces scalability limitations. These constraints stem from two factors (1) complexity caused by contingencies in IEGS that span multiple time steps, and (2) slow convergence of VC-AM in specific scenarios. Additionally, the proposed N-1 contingency evaluation framework focuses on preventive evaluation and excludes protective actions during contingency propagation. To address these gaps, future work will focus on (1) identifying contingency propagation speed to avoid unnecessary computation demand, (2) developing robust algorithms to accelerate convergence iterations, and (3) incorporating protective actions into cyber-physical security analysis to capture the post-contingency states more accurately.

REFERENCES

- [1] A. Mazza, E. Bompard and G. Chicco, "Applications of power to gas technologies in emerging electrical systems", *Renew. Sust. Energy Rev.*, vol. 92, pp. 794-806, 2018.
- [2] European Commission, "EU energy policy-energy system integration", https://energy.ec.europa.eu/topics/energy-systems-integration_en, 2018.
- [3] U.K. gov., "Energy secretary takes action to reinforce UK energy supply," <https://www.gov.uk/government/news/energy-secretary-takes-action-to-reinforce-uk-energy-supply>, 2024.
- [4] Ed Miliband, "National Energy System Operator (NESO) launches on 1 October," <https://www.neso.energy/news/national-energy-system-operator-neso-launches-1-october>, 2024.
- [5] S. Zhang, G. Pan, B. Li, et al, "Multi-timescale security evaluation and regulation of integrated electricity and heating system," *IEEE Trans. Smart Grid*, doi: 10.1109/TSG.2024.3493818.
- [6] N. Malik, R. Collins, and M. Vamburkar, "Cyber-attack pings data systems of at least four gas networks," <https://www.bloomberg.com/news/articles/2018-04-03/dayafter-cyber-attack-a-third-gas-pipe-data-system-shuts>, 2018.
- [7] A. Sawas, H. Khani, and H. Farage, "On the resiliency of power and gas integration resources against cyber attacks," *IEEE Trans. Ind. Inf.*, vol. 17, no. 5, pp. 3099-3110, 2021.
- [8] BBC News, "People will die in storm power cuts, councillor says," <https://www.bbc.co.uk/news/articles/cdjgy32z114o>, 2024.
- [9] G. Cao, W. Gu, P. Li, et al, "Operational risk evaluation of active distribution networks considering cyber contingencies," *IEEE Trans. Ind. Inf.*, vol. 16, no. 6, pp. 3849-3861, 2020.
- [10] C. Wang, M. Yan, K. Pang, et al, "Cyber-physical interdependent restoration scheduling for active distribution network via ad hoc wireless communication," *IEEE Trans. Smart Grid*, vol. 14, no. 5, pp. 3413-3426, 2023.
- [11] C. Vellaithurai, A. Srivastava, S. Zonouz, et al, "CPIndex: cyber-physical vulnerability assessment for power-grid infrastructures," *IEEE Trans. Smart Grid*, vol. 6, no. 2, pp. 566-575, 2015.
- [12] M. Bahrami, M. Firuzabd, and H. Farzin, "Reliability evaluation of power grids considering integrity attacks against substation protective IEDs," *IEEE Trans. Ind. Inf.*, vol. 16, no. 2, pp. 1035-1044, 2020.
- [13] N. Jacobs, S. Hossain, and A. Summers, "Modeling data flows with network calculus in cyber-physical systems: enabling feature analysis for anomaly detection applications," *Information*, vol. 12, 255, 2021.
- [14] H. Yang, L. Cheng, and X. Ma, "Combining measurements and network calculus in worst-case delay analyses for networked cyber-physical systems," *IEEE Infocom*, 2019.
- [15] A. Salehpour, I. Al-Anbagi, K. Yow, et al, "Modeling cascading failures in coupled smart grid networks," *IEEE Access*, vol. 10, pp. 81054-81070, 2022.
- [16] M. Zhou, C. Liu, A. Jahromi, et al, "Revealing vulnerability of N-1 secure power systems to coordinated cyberphysical attacks," *IEEE Trans. Power Syst.*, vol. 38, no. 2, pp. 1044-1057, 2023.
- [17] X. Xu, K. Xiahou, W. et al, "Security assessment of cascading failures in cyber-physical power systems with wind power penetration," *IEEE Trans. Power Syst.*, 2025.
- [18] S. Bada, M. Ehsan, M. Shahidehpour, et al, "Security-constrained unit commitment with natural gas pipe transient constraints," *IEEE Trans. Smart Grid*, vol. 11, no. 1, pp. 118-128, 2020.
- [19] S. Zhang, W. Gu, X. Zhang, et al, "Towards fast and robust simulation in integrated electricity and gas system: a sequential united method," *IEEE Trans. Power Syst.*, vol. 39, no. 1, pp. 1822-1836, 2024.
- [20] P. Alluri, H. Banna, M. Khalghani, S. Solanki and J. Solanki, "Real-time framework for monitoring cyber disruptions in power grids," *IEEE Trans. Indus. Infor.*, vol. 18, no. 6, pp. 4008-4017, 2022.
- [21] S. Zhang, S. Chen, W. Gu, et al, "Dynamic optimal energy flow of integrated electricity and gas systems in continuous space," *Appl. Energy*, vol. 375, 124052, 2024.
- [22] S. Gharebaghi, N. Chaudhuri, T. He, et al, "Dynamic modeling and mitigation of cascading failures in power grids with interdependent cyber and physical layers," *IEEE Trans. Smart Grid*, vol. 15, no. 3, pp. 3235-3247, 2024.
- [23] S. Zhang, W. Gu, X. Zhang, et al, "Dynamic modeling and simulation of integrated electricity and gas systems", *IEEE Trans. Smart Grid*, vol. 99, no. 99, pp. 1011-1026, 2023.
- [24] Y. Dong, H. Guan, J. Zeng, et al, "Evaluation of gas release rate through holes in pipes," *J. Loss Prev. Process Ind.*, vol. 15, no. 6, pp. 423-428, 2002.
- [25] J. Zhu, G. Xu, "A unified model and automatic contingency selection algorithm for the P and Q subproblems," *Elec. Power Syst. Res.*, vol. 32, pp. 101-105, 1995.
- [26] S. Zhang, et al, "Case data for CP-IEGS," https://www.researchgate.net/publication/387522435_Case_data_for_CP-IEGS, 2024.
- [27] J. Fang, Q. Zeng, M. Ai, et al, "Dynamic optimal energy flow in the integrated natural gas and electrical power systems," *IEEE Trans. Sust. Energy*, vol. 9, no. 1, pp. 188-198, 2018.
- [28] S. Zhang, et al, "1000 random datasets for CP-IEGS," https://www.researchgate.net/publication/391987951_1000_random_datasets_for_CP-IEGS, 2025.



Suhan Zhang (Member, IEEE) received his B.S. and Ph.D degrees in electrical engineering from North China Electric Power University, China, in 2018 and Southeast University, China, 2023. He currently works as a postdoc research associate at the School of Electrical and Electronic Engineering, The University of Sheffield. His research interests include modeling, simulation and operation of cyber-physical energy systems.



Xin Zhang (Senior Member, IEEE) received the B.Eng. degree in automation and control systems from Shandong University, China, in 2007, and the M.Sc. and Ph.D. degrees in electrical power engineering from The University of Manchester, U.K., in 2007 and 2010, respectively. He is currently a Professor of control and power systems with the University of Sheffield, U.K. From 2011 to 2019, he was with National Grid Electricity System Operator, Wokingham, U.K. From 2019 to 2021, he was a Senior Lecturer with Cranfield University, U.K. From 2021 to 2023, he was an Associate Professor with Brunel University London, U.K. His research interests include power system control and operation, cyber-physical power systems modeling and digital simulation, and grid-integrated transport electrification. He serves as an Associate Editor for IEEE Transactions on Smart Grid, IEEE Power Engineering Letters, Protection and Control of Modern Power Systems, Energy Conversion and Economics, and Cyber-physical Energy Systems. He was the recipient of the U.K. Research and Innovation Future Leaders Fellowship in 2022.



Rui Zhang received the Ph.D degree in electrical and electronic engineering from The University of Manchester, U.K., in 2012. He is currently a Technical Policy Manager, playing a vital role in shaping policies and strategies for the National Energy System Operator, U.K. He has strong background in power system control and operation. His research interests include a wide range of areas such as zero-carbon operation and whole energy system operation optimisation.



Wei Gu (Senior Member, IEEE) received his B.S. and Ph.D. degrees in Electrical Engineering from Southeast University, China, in 2001 and 2006, respectively. He is now a professor at the School of Electrical Engineering, Southeast University. He is the director of the institute of distributed generations and active distribution networks. His research interests include distributed generations and microgrids, integrated energy systems. Dr. Gu is an Editor for the IEEE Transactions on Power Systems, IEEE Power Engineering Letters, CSEE JPES.



Ge Cao (Member, IEEE) received the B.S. and Ph.D. degrees in electrical engineering from Southeast University, Nanjing, China, in 2015 and 2021, respectively. He is currently a lecturer of Electrical Engineering with the School of Electrical Engineering, Xi'an University of Technology. His research interests include distributed generations and microgrids.